JAAS

PAPER

View Article Online
View Journal

Check for updates

Cite this: DOI: 10.1039/d2ja00021k

High-throughput single pixel spectral imaging system for glow discharge optical emission spectrometry elemental mapping enabled by compressed sensing†

Gerardo Gamez, * Yue She, Paola Rivera, Songyue Shi and Kevin Finch

Glow discharge optical emission spectroscopy elemental mapping (GDOES EM), enabled by spectral imaging strategies, is an advantageous technique for direct multi-elemental analysis of solid samples in rapid timeframes. Here, a single-pixel, or point scan, spectral imaging system based on compressed sensing image sampling, is developed and optimized in terms of matrix density, compression factor, sparsifying basis, and reconstruction algorithm for coupling with GDOES EM. It is shown that a 512 matrix density at a compression factor of 30% provides the highest spatial fidelity in terms of the peak signal-to-noise ratio (PSNR) and complex wavelet structural similarity index measure (cw-SSIM) while maintaining fast measurement times. The background equivalent concentration (BEC) of Cu I at 510.5 nm is improved when implementing the discrete wavelet transform (DWT) sparsifying basis and Two-step Iterative Shrinking/Thresholding Algorithm for Linear Inverse Problems (TwIST) reconstruction algorithm. Utilizing these optimum conditions, a GDOES EM of a flexible, etched-copper circuit board was then successfully demonstrated with the compressed sensing single-pixel spectral imaging system (CSSPIS). The newly developed CSSPIS allows taking advantage of the significant cost-efficiency of point-scanning approaches (>10× *vs.* intensified array detector systems), while overcoming (up to several orders of magnitude) their inherent and substantial throughput limitations. Ultimately, it has the potential to be implemented on readily available commercial GDOES instruments by adapting the collection optics.

Received 19th January 2022
Accepted 18th February 2022

DOI: 10.1039/d2ja00021k

rsc.li/jaas

Published on 18 February 2022. Downloaded by Texas Tech University on 3/16/2022 9:08:21 PM.

1. Introduction

Mapping the distribution of elements in solid samples is critical for understanding the underlying mechanisms of natural and engineered materials.[1–7] There are several elemental mapping (EM) techniques currently available but, while they possess different advantages, a common limitation is long acquisition times, which can require several hours or more. Glow discharge optical emission spectroscopy (GDOES) has been shown to permit EM from within the sputtered area when operated in pulsed power mode and sustained under higher-than-typical pressures.[8–15] Leveraging the inherent GDOES advantages of direct solid sampling, simultaneous multi-elemental analysis, fast sputtering rates, multi-matrix calibration schemes, and depth profiling in the nm scale, results in ultra-high throughput elemental mapping capabilities that can be several orders-of-magnitude faster *vs.* typical techniques.[2,11,16]

One of the aspects that enables GDOES EM is its coupling to an appropriate spectral imaging system for data collection, with several embodiments reported. On the one hand, wavelength-scan approaches, also known as staring-camera type, allow measuring monochromatic images one wavelength at a time, with the advantage of giving access to both spatial dimensions simultaneously. The wavelength selection device used influences greatly the GDOES EM performance: a monochromator gives access to a wide λ range but λ-scan is slow and it compromises light-throughput *vs.* spectral resolution;[8,9] a dichroic filter is very cost effective and can have a large numerical aperture (NA) but the λ range and spectral resolution for each filter are very limited, such that tens of filters would be needed for multi-elemental analysis;[14] acousto-optic tunable filters give fast random λ access and can also have a large NA but they have limited λ range and UV capabilities, spectral resolution that varies with λ, and can be costly.[15] On the other hand, line-scan approaches, also known as push-broom type, allow measuring one spatial dimension and the λ dimension simultaneously while the remaining spatial dimension has to be scanned. Reported grating spectrograph line-scan systems used for GDOES EM have shown large NA, a wide λ range that could potentially be extended into VUV, and fast hyperspectral

Texas Tech University, Department of Chemistry and Biochemistry, Lubbock, TX 79409-41061, USA. E-mail: gerardo.gamez@ttu.edu; Tel: +1 806 834-8946

† Electronic supplementary information (ESI) available. See DOI: 10.1039/d2ja00021k

Published on 18 February 2022. Downloaded by Texas Tech University on 3/16/2022 9:08:21 PM.

imaging capabilities.[10–13] One type of spectral imaging system that has not yet been demonstrated with GDOES EM is the point-scan approach, or single-pixel imaging system (SPIS). The main reason is that the typically required scanning in the two spatial dimensions leads to significantly slower data acquisition. However, the use of a single pixel detector is the most hardware cost-effective approach, by at least an order of magnitude, in contrast to the 2D array detectors necessary for GDOES EM with the line- or wavelength-scanning approaches.

Compressed sensing (CS) is a sampling scheme that allows reconstruction of signals with only a fraction of the samples required by the Nyquist theorem, thus allowing for much faster data acquisition.[17–27] The principles that enable CS are: group sampling, which allows obtaining more information per sample and inherent multiplex advantages; incoherence, which translates into random selection of groups for sampling to avoid bias and improve the probability of including all required components in less measurements; and data sparsity, which refers to having most of the signal information contained in only a few components, or ample redundant information, such that the data is compressible. Thus, several CS based approaches have been demonstrated for allowing much faster data acquisition in single-pixel imaging systems.[28–34]

Herein, a CSSPIS, based on a digital micromirror device (DMD) spatial modulator, is developed and adapted for GDOES EM. The effects of the operating and image reconstruction parameters are studied with respect to the image fidelity performance and the optimized operating conditions are demonstrated with GDOES EM. This will enable taking advantage of the SPIS significant cost-effectiveness and make GDOES EM more accessible, while allowing for much faster throughput compared to its traditional SPIS counterpart. An additional potential advantage is that this approach opens the possibility to perform EM on commercial GDOES systems, typically featuring single-pixel detectors, by adapting the optical collection path with a spatial modulator.

2. Experimental

Compressed sensing single pixel spectral imaging system

The GD lamp, previously described in,[9] was adapted with a 9 mm cathode sputtering diameter. The GD was operated under UHP Ar gas (99.999%) flowing at a rate of 0.15 L min^{-1} controlled by a mass flow controller (Apex, AX-MC-1SLPM-D/5M) and in conjunction with a roughing pump (Edwards, RV12), resulted in a pressure of 14 Torr monitored by a pressure gauge (MKS, 901P-11040). The RF power supply (Dressler, Cesar 1350) was pulsed at 1 kHz and 4% duty cycle, and the forward power was adjusted to ~350 W with the reflected power <5 W. A chiller (Thermo Scientific, Neslab Merlin M25) cooled the RF power supply, impedance matching network, and GD backing electrode.

Fig. 1A shows how the light from the GD was collected with a series of plano-convex singlet lenses (Thorlabs, fused silica, 2 inch diameter, 200 mm focal length). L1 collimates the light towards a flat dielectric mirror (Thorlabs, fused silica, BB3-E02) that reflects it to L2, which focuses the light onto the DMD (Texas Instruments, DLP® LightCrafter™ Evaluation Module with DLP 0.3 WVGA chipset). L3 then collimates the encoded light from the DMD and L4 focuses the light onto the entrance slit of the monochromator (Chromex, Model 500iS/SM, linear dispersion 1.6 nm mm^{-1}), which was open to the maximum width of 2 mm. The exit slit width was also completely open to 2 mm and a PMT (Hamamatsu, R928P), connected to a high voltage power supply (Bertan, 230-05R), was used for detection.

The PMT output was split in two with the first part connected to a low noise amplifier (Stanford Research Systems, Model SR570) followed by a low-pass filter (KROHN-HITE, Model 3342) and digitized by DAQ (National Instruments, USB-6259), while the second part was connected to a home-built amplifier and digitized by another DAQ (National Instruments, USB-6001). The purpose of this was for measuring the full dynamic range with a low-gain branch, which is advantageous for measuring the baseline and the highest intensities resulting from just a few selected encoding masks, *i.e.* matrices. However, most of the matrices will yield similar intensities, thus using the high-gain branch allows "zooming-in" around these intensities and enables to better distinguish the differences that contain most of the information, but the few highest intensity data will appear saturated in this case.

Image encoding

Fig. 1B and C show the experimental timing diagram. The DMD was setup as a second monitor to a computer, such that it projected a video consisting of a sequence of encoding matrices. These video sequences of Scrambled Block Hadamard Ensemble (SBHE) structurally random matrices (SRM) were produced as previously described.[28] Different video sequences were produced at various matrix densities, including 512, 1024, 2048, and 4096. In short, the image size is 256 × 256 pixels, for a total of 65 536 pixels. The matrix density refers to number of DMD pixels that simultaneously reflect parts of the image towards the detector, where their respective intensities are combined. In addition, video sequences at different compression factors were also produced, including 10%, 20%, 30%, 40%, 50%, and 100%. The compression factor refers to the fraction of measurements/combinations used to reconstruct the image with respect to the ones required by the Nyquist theorem, or in a determined system of equations, which would correspond to 65 536 for 100% in our case. During all video sequences, each different encoding matrix was projected (ON) for ~66 ms, followed by a blank matrix (OFF) projected for ~33 ms that served to block the GD emission from reaching the monochromator. This effectively results in a sequence of baseline resolved intensity peaks that enable improved analysis and processing of GDOES intensity data collected for each matrix.[28]

Data analysis

The data analysis and processing consists of several steps. Essentially, the intensity of each matrix combination is averaged over its ON time and extracted into a single file. Next, the low-gain and high-gain intensity data are combined by

 This journal is © The Royal Society of Chemistry 2022

Published on 18 February 2022. Downloaded by Texas Tech University on 3/16/2022 9:08:21 PM.

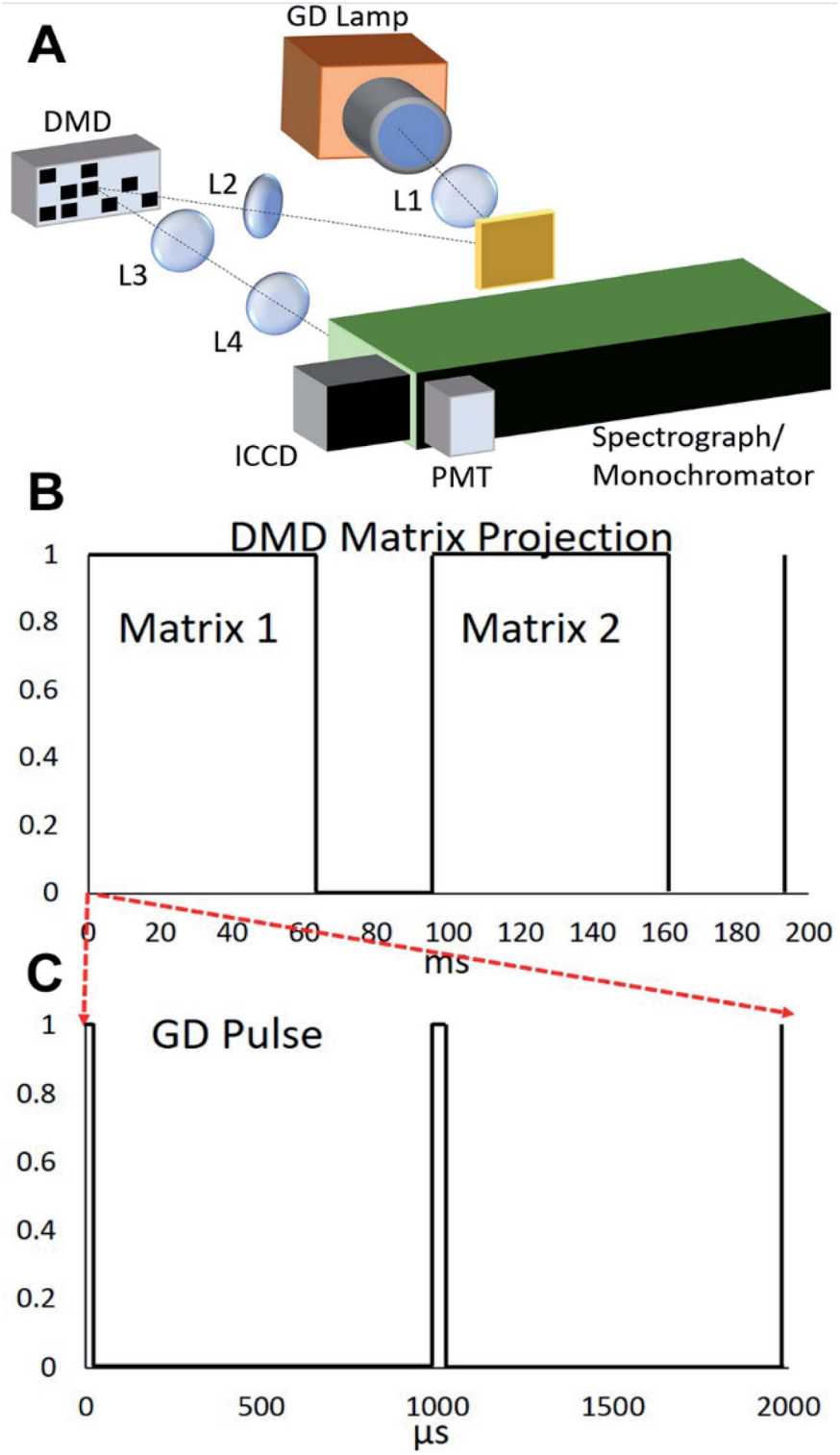

Fig. 1 (A) Schematic of the instrument setup for CSSPIS from GDOES EM where the light is imaged onto the DMD spatial modulator and the resulting encoded image is refocused into the monochromator. The experimental timing showing (B) the DMD projection period and (C) the GD pulsing frequency. Note the different time scales of each plot. See Experimental section for further details.

matching the different scales, which allows replacing the saturated intensities in the high-gain data set with the unsaturated ones in the low-gain set. Then, if necessary, baseline and amplitude drift corrections are applied, where a small set of identical encoding matrices, applied before the beginning and after the end of the measurement, are used to assess the drift. Finally, two CS algorithms, selected for their speed advantages,[35] were implemented for image reconstruction, including

Published on 18 February 2022. Downloaded by Texas Tech University on 3/16/2022 9:08:21 PM.

Two-step Iterative Shrinking/Thresholding Algorithm for Linear Inverse Problems (TwIST)[36] and Gradient Projection for Sparse Reconstruction (GPSR).[37] In addition, two different sparsifying basis, including 9–7 discrete wavelet transform (DWT) and discrete cosine transform (DCT), were utilized. The reconstructed images were median filtered (12 × 12 block size) and the intensity scale normalized to 16 bit.

3. Results & discussion

The model sample used for studying the effect of the operating/reconstruction conditions on GDOES EM CSSPIS was a nickel (75.2%)/chromium (19.4%) alloy substrate (NIMONIC alloy 75, E3918, 0.005% copper) with pure copper wire surface inserts of 1 mm diameter, separated by 1 mm edge-to-edge (Fig. 2A). Fig. 2B shows an end-on picture of the sample in the chamber while the GD is in operation (plasma ON). Given the slit width limitations of the monochromator, only part of the GDOES image projected on to the DMD made it through to the PMT detector, which is highlighted by the red rectangle in Fig. 2A. Fig. 2C to H show samples of reconstructed spectral images under selected conditions. It is evident that the image quality improves as more measurements are obtained, or at higher compression factor percentages, particularly from 10% to 30% while higher percentages yield diminishing returns.

Fidelity assessment

The fidelity of the spectral images obtained with the CSSPIS was quantified by two methods: the more typical peak signal-to-noise ratio (PSNR) method and the complex wavelet structural similarity index measure (cw-SSIM). The PSNR method calculates the mean squared error (MSE) by doing a pixel-to-pixel comparison between the image of interest and a standard image. This is followed by weighing the MSE with the maximum possible pixel value and expressing the result in decibels, where higher PSNR values indicate improved fidelity. While the PSNR

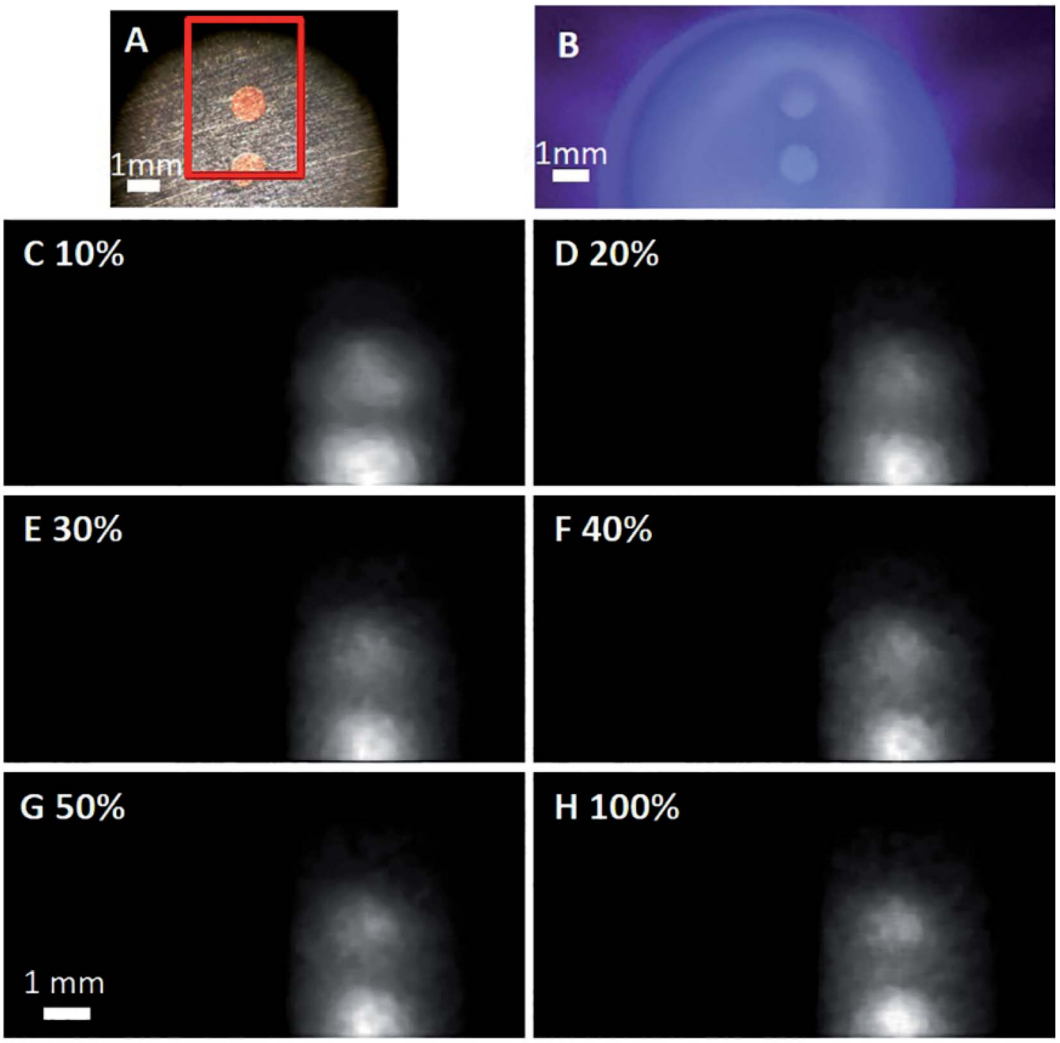

Fig. 2 (A) Model sample of stainless steel SRM with pure copper inserts. (B) End-on view of mounted model sample during GD operation (plasma ON). (C–H) Reconstructed images obtained with the CSSPIS from GDOES EM of the model sample at 510.5 nm, Cu I, under different compression factors (matrix density 512, DWT, TwIST).

 This journal is © The Royal Society of Chemistry 2022

Published on 18 February 2022. Downloaded by Texas Tech University on 3/16/2022 9:08:21 PM.

metric has several advantages, including that is simple to compute, it is a global measure that is not very well suited to assess perceived visual quality.[38] For example, the PSNR value will be significantly affected if the image of interest is exactly the same as the standard image but just shifted a couple of pixels.

The SSIM method is a slightly more involved calculation but gives a better assessment of perceived visual quality.[38,39] In this case, the interdependency of nearby pixels is taken into account by only focusing on a small window section, or local group of pixels, of the image-of-interest (x) and the corresponding one in the standard image (y) at any given time. It compares luminance (l, or brightness, measured as the average intensity, μ), contrast (c, measured as standard deviation, σ), and structure (s, measured as cross correlation of x and y after mean removal, σ_{xy}) between the small image sections:[38]

$$S(x,y) = l(x,y)c(x,y)s(x,y) = \left(\frac{2\mu_x\mu_y + C_1}{\mu_x{}^2 + \mu_y{}^2 + C_1}\right)\left(\frac{2\sigma_x\sigma_y + C_2}{\sigma_x{}^2 + \sigma_y{}^2 + C_2}\right)\left(\frac{2\sigma_{xy} + C_3}{\sigma_x\sigma_y + C_3}\right)$$

where C_1, C_2 and C_3 are small positive constants to stabilize near zero values. The small window section is then shifted pixel-by-pixel across the image to yield an SSIM map and the total SSIM score is obtained by averaging all the SSIM map values. The total SSIM values are expressed in a zero to 1 scale, where values closer to 1 indicate higher fidelity.

The results of the fidelity assessment for the 512 matrix density as a function of compression factor are shown in Fig. 3. It should be noted that only the part of the image that made it through the monochromator entrance slit (brighter part of Fig. 2C–H, corresponding to the red box highlight of Fig. 2A) was taken into account for the comparison. In general, the PSNR values improve from ~28 db at 10% compression factor to ~32 db at 30%. On the other hand, the PSNR stays constant from 30% to 50% compression factor. The SSIM shows a similar trend, with values improving from ~0.85 at 10% to ~0.9 at 30%, where they reach a plateau. Interestingly, the effect of the algorithm, or sparsifying basis, used during the reconstruction is indistinguishable within the experimental error for both fidelity quantification methods. These general trends change gradually as the matrix density is increased to 1024 (Fig. S1†), 2048 (Fig. S2†), and ultimately 4096 (Fig. 4). For example, the PSNR values keep increasing as a function of compression factor, with no evident plateau, and with a steeper slope at higher matrix densities. Furthermore, the overall PSNR values obtained are worse as the matrix density is increased, particularly at lower compression factors. It is also worth noting that the choice of sparsifying basis and reconstruction algorithm start to have an increasingly significant effect at higher matrix densities.

The GPSR algorithm, as well as DCT sparsifying basis, performs better at lower compression factors and increased matrix densities. This is particularly evident at 4096 (Fig. 4) where a paired data t-test (2-tail, significance = 0.05) including all compression factors gives a p-value of 1.6×10^{-3} for DCT

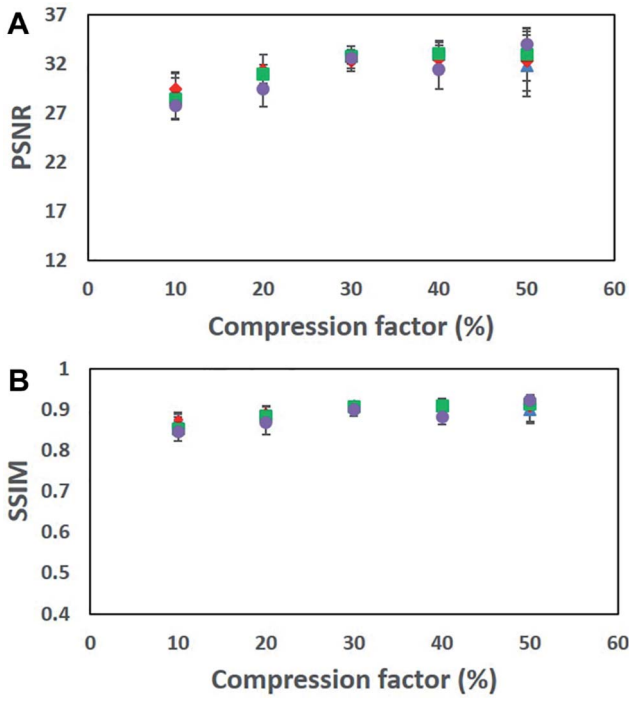

Fig. 3 Fidelity characterization, in terms of PSNR (A) and SSIM (B), of GDOES EM CSSPIS reconstructed images at 512 matrix density as a function of compression factor. The effect of the sparsifying basis/reconstruction algorithm were also studied: DCT/TwIST (◆), DWT/TwIST (●), DCT/GPSR (▲), DWT/GPSR (■).

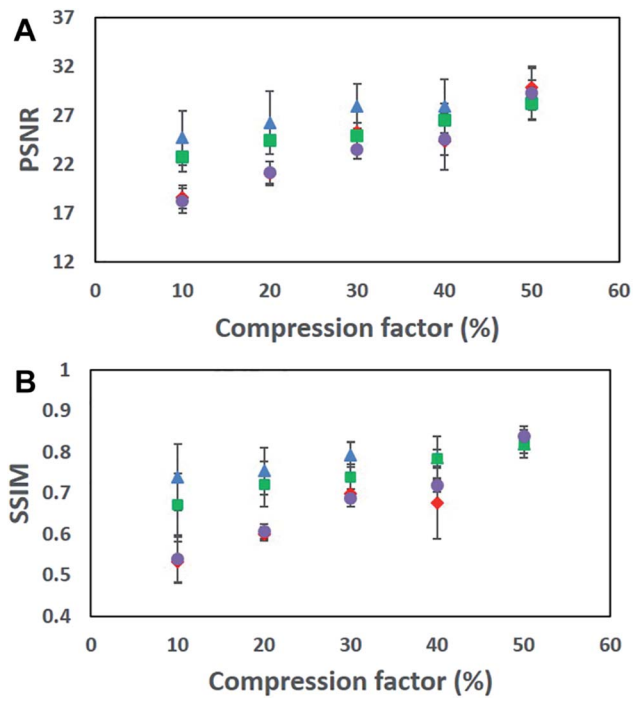

Fig. 4 Fidelity characterization, in terms of PSNR (A) and SSIM (B), of GDOES EM CSSPIS reconstructed images at 4096 matrix density as a function of compression factor. The effect of the sparsifying basis/reconstruction algorithm were also studied: DCT/TwIST (◆), DWT/TwIST (●), DCT/GPSR (▲), DWT/GPSR (■).

Published on 18 February 2022. Downloaded by Texas Tech University on 3/16/2022 9:08:21 PM.

and 1.1×10^{-3} for DWT, to confirm GPSR outperforms TwIST. In addition, when GPSR is used, DCT outperforms DWT (p-value 1.8×10^{-2}). On the other hand, the effect of algorithm and basis starts to once again become indistinguishable when the number of measurements is increased to 50% compression factor. It is instructive to see that the visual perception-based SSIM at 4096 matrix density shows a similar trend. The better performance of GPSR *vs.* TwIST is more evident here (p-values of 9.2×10^{-6} for DCT, and 3.1×10^{-5} for DWT), but DCT outperforms DWT only up to 30% compression factor (p-values of 1.3×10^{-2} for GPSR, and 1.5×10^{-3} for TwIST), which also put into perspective the more abstract PSNR values.

The better performance of the 512 matrix density has to do with the corresponding matrix signal and its precision. As mentioned above, the matrices, or encoding masks, displayed on the DMD enable combining the intensities of several parts of the image at the PMT detector. Each matrix is a different combination so it is critical to be able to distinguish between the different resulting intensities. When less parts of the image are combined (512 matrix density) the differences between the corresponding matrix measured intensities are larger, such that it is easier to distinguish the differences under a particular set of signal and standard deviation conditions. As more parts of the image are combined (up to 4096 matrix density) the differences become gradually smaller, such that the inherent signal and noise conditions play a more important role, thus making them harder to distinguish.

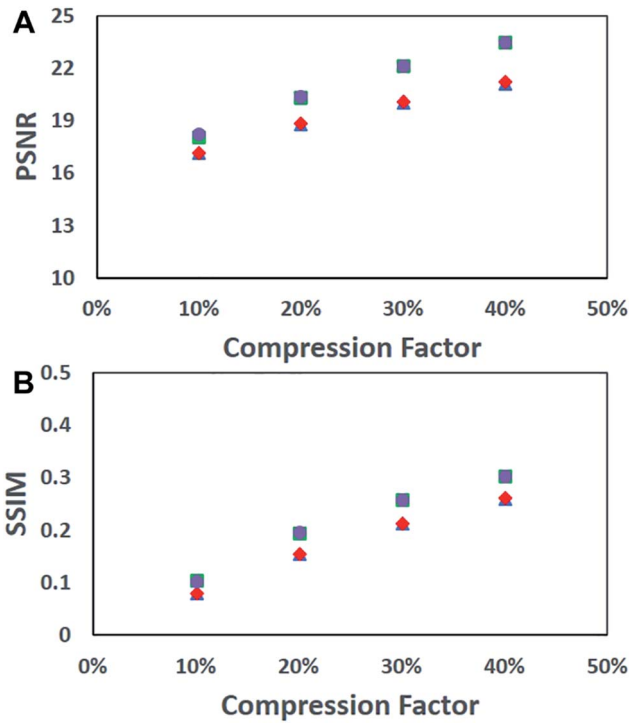

Fig. 5 Fidelity characterization, in terms of PSNR (A) and SSIM (B), of computer simulated CSSPIS reconstructed images at 512 matrix density as a function of compression factor. The effect of the sparsifying basis/reconstruction algorithm were also studied: DCT/TwIST (◆), DWT/TwIST (●), DCT/GPSR (▲), DWT/GPSR (■).

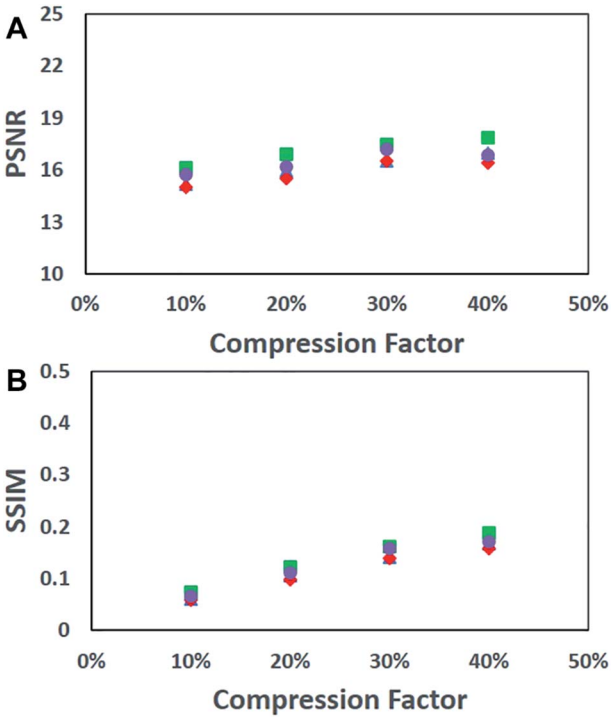

Fig. 6 Fidelity characterization, in terms of PSNR (A) and SSIM (B), of computer simulated CSSPIS reconstructed images at 4096 matrix density as a function of compression factor. The effect of the sparsifying basis/reconstruction algorithm were also studied: DCT/TwIST (◆), DWT/TwIST (●), DCT/GPSR (▲), DWT/GPSR (■).

Of course, there is a compromise between matrix intensity differences and the brightness of the light source being studied. For example, under very low light level conditions the overall signal-to-noise (SNR) level from the combinations coming from the smaller density matrices may start to become inadequate,

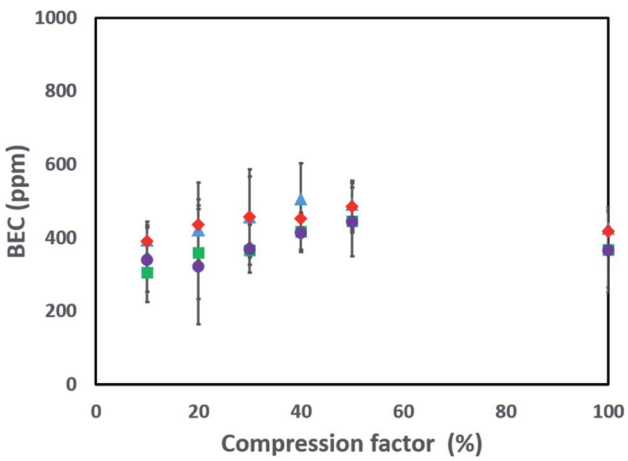

Fig. 7 Background equivalent concentration (BEC) of copper (Cu I, 510.5 nm) from GDOES EM CSSPIS reconstructed images of the model sample at 512 matrix density as a function of compression factor. The effect of the sparsifying basis/reconstruction algorithm were also studied: DCT/TwIST (◆), DWT/TwIST (●), DCT/GPSR (▲), DWT/GPSR (■).

This journal is © The Royal Society of Chemistry 2022

Published on 18 February 2022. Downloaded by Texas Tech University on 3/16/2022 9:08:21 PM.

leading to worse performance compared to higher matrix densities, as shown in.[28]

Computer simulations of the CSSPIS process were performed to better understand the observed trends. In this case, the CameraMan image was used and noise was added with the MATLAB function "awgn" (adds white Gaussian noise to signal) at a ratio of signal power to noise power of 50 dbW, thus simulating source noise (Fig. S3†). The image was multiplied sequentially by each matrix (binary, 1 and 0) in the corresponding series, and the pixel values in each resulting image were integrated. This was followed by the image reconstruction method described in the Data Analysis section above. Fig. 5 (512 matrix density) and Fig. 6 (4096 matrix density), as well as S4 (1024) and S5 (2048), show the PSNR and SSIM as a function of compression factor for the simulation experiments. While the absolute PSNR and SSIM values are not comparable, the trends are very instructive. For example, there is a general improved performance with increased percentages, which is consistent with the experimental data. Also, the performance of the 512 matrix density, as evidenced by the higher PSNR and SSIM values, is better compared to the 4096 matrix. This is again consistent with the experimental data. The trends with respect

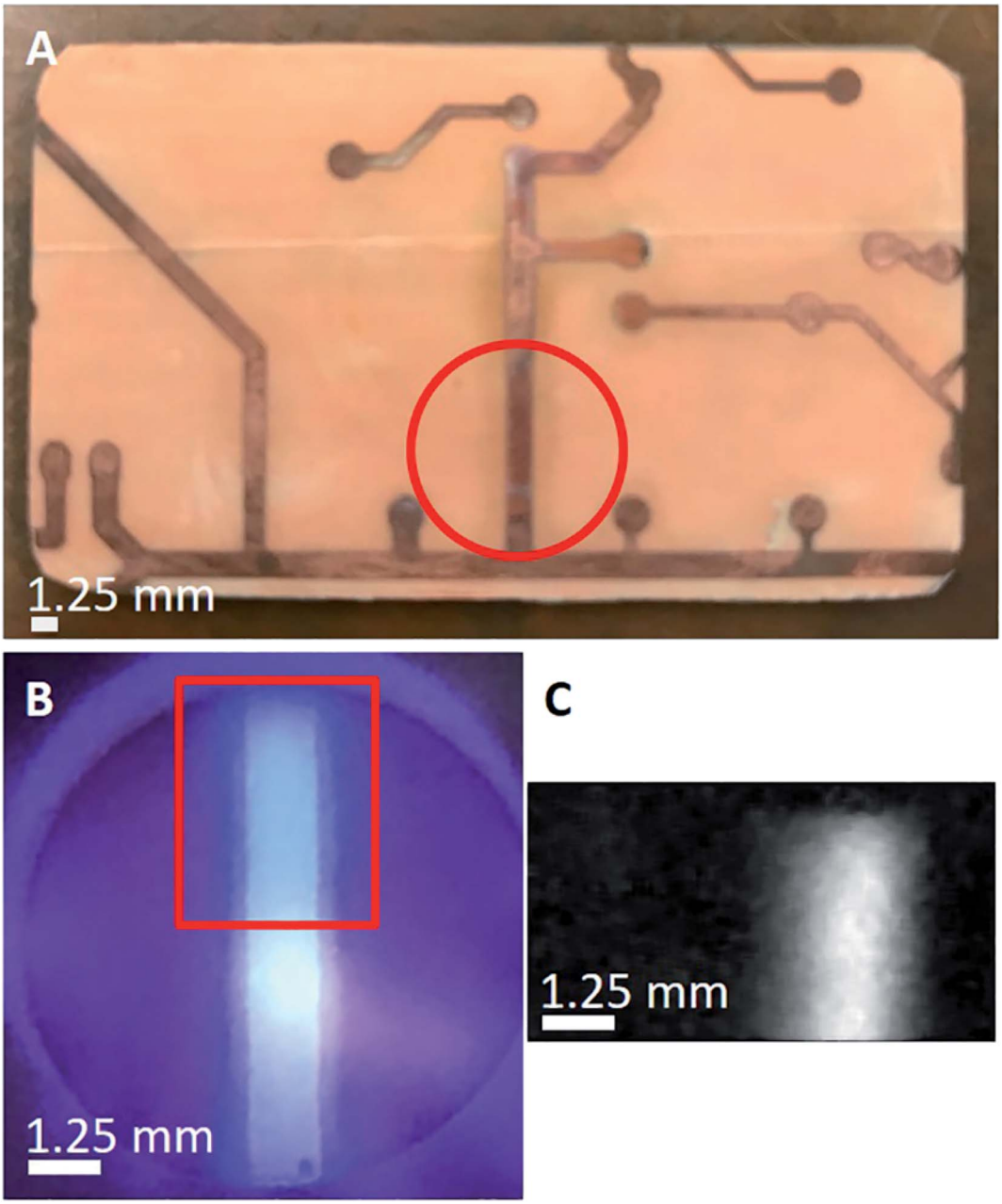

Fig. 8 (A) Etched copper flexible electrical board sample, with red circle showing area samples by GD. (B) End-on view of mounted copper-board sample during GD operation, with red rectangle showing area imaged by the CSSPIS. (C) GDOES EM of copper (Cu I, 510.5 nm) with CSSPIS under optimized conditions of 512 matrix density, 30% compression factor, DWT sparsifying basis, and TwIST reconstruction algorithm.

Published on 18 February 2022. Downloaded by Texas Tech University on 3/16/2022 9:08:21 PM.

to effect of the reconstruction algorithm or sparsifying basis are not the same, which may be due to the experimental data containing both source and detector noise, while the simulated data only has source noise added.

An important aspect to consider is how these parameters would affect the quantitative elemental analysis. Thus, the images reconstructed from the data obtained with the optimum 512 matrix density were used to calculate background equivalent concentrations (BEC), of the copper inserts (Fig. 7):

$$\mathrm{BEC} = \frac{0.01 \times k \times \mathrm{RSDB} \times C_0}{\mathrm{SBR}}$$

where the constant $k = 3$, RSDB is the relative standard deviation of the background, SBR is the signal to background ratio, and C_0 is the copper insert concentration at 99%. The signal was averaged over the copper insert area, while the background was averaged over a comparable area on the substrate.

It is interesting to note that in general the BEC value increases, or becomes worse, from 10% compression factor compared to 40% (p-value 3.3×10^{-3}). This trend can be explained by looking at Fig. 1, where the images recovered at 10% look smoothed, or blurred, compared to 40%, which results in lower RSDB values and translates into a lower BEC at 10%. The BEC decreases again when comparing 40% to 100% (p-value 2.8×10^{-2}), but this is due to higher SBR at 100%. In addition, DWT gives better, or lower, BECs compared to DCT (paired data t-test, 2 tail, including all compression factors) with p-values of 2.2×10^{-5} for GPSR, and 3.9×10^{-4} for TwIST. The BEC values are estimates of detection limits and here they are one to two orders of magnitude higher compared to typical ones reported for GDOES bulk analysis, due to several factors. First, the use of higher operating pressures here leads to lower sputtering rates and corresponding lower emission signals. Nonetheless, this change is expected to be less than an order of magnitude. Second, and most important, the detection limits in bulk analysis are achieved by integrating the signal for up to 10 s under continuous GD power. On the other hand, the PMT here was allowed to collect light for ~0.066 s during each matrix measured. However, the GD power is pulsed at 1 kHz with a 4% duty cycle, which lowers the time the GD signal is actually collected to 0.00264 s per matrix. Furthermore, one has to take into account the number of times the same DMD pixel is included in the total measurement, which comes out to ~154 by using the matrix density (512), image pixel density (256×256) and compression factor (0.3). Thus, the total time in which signal is collected per pixel in the complete measurement here is ~0.4 s, compared to the 10 s typically used for bulk analysis, which helps to explain the difference in detection limits, together with the lower sputtering rates at the higher pressures. A similar effect on detection limits is observed when performing GDOES depth profiling studies where the signal is integrated for much shorter times, ~0.1 s, compared to bulk analysis.

Finally, GDOES EM of a flexible, etched-copper board sample was successfully demonstrated with the optimized CSSPIS (Fig. 8). A matrix density of 512 was implemented because it proved to be optimum in terms of spatial fidelity at the lower 30% compression factor to permit the fastest measurement. Also, the DWT sparsifying basis and TwIST reconstruction algorithm were used because they showed better BEC values. The CSSPIS measurement is significantly faster compared to typical SPIS systems relying on pixel-to-pixel rastering. In fact, the improved measurement time is not linear, as the 30% value would suggest, because the intensities from many pixels, 512 in this case, are combined at any given measurement. This multiplexing yields a significant improvement in SNR ratio at the detector compared to single pixel rastering systems and provides for considerably faster data acquisition times. The enhancement would correspond to the improvement in SNR, which is ~ equivalent to the number of combined pixels (more than two orders-of-magnitude), when the noise is detector limited. The actual measurement time for the data shown in Fig. 8 is ~32 min, which is already competitive with other elemental mapping techniques. On the other hand, it is at least an order of magnitude slower compared to the time required by GDOES EM using line- or wavelength-scan spectral imaging techniques. However, the current measurement time here is limited by implementing the DMD as a second monitor (and corresponding relatively-slow refresh rate), the pulsed GD power duty cycle, and the signal averaging during the time the matrix is projected, which results in a "dilution" of 4% signal in 96% background. Uploading significantly shorter matrix series directly into the limited DMD memory would permit much faster refresh rates and to implement DMD-based synchronized detection strategies, as demonstrated for LIBS,[40] making the current matrix OFF-time unnecessary and enabling a significantly improved SBR and lateral resolution.[9] Such improvements would allow significantly faster acquisition times at similar LODs or better LODs at similar acquisition times.

4. Conclusions

A CSSPIS has been tailored and implemented to GDOES EM for the first time, with optimization from actual GD plasma emission. In terms of spatial fidelity, the addition of a SSIM assessment to the PSNR has allowed a better understanding of the reconstructed images in terms of visual perception. The best fidelity performance displayed by the 512 matrix density can be attributed to the greater differences in peak intensity measured for each of the encoded matrices, where a compression factor of 30% already yields optimum results. The quantitative performance, in terms of BEC, shows the DWT sparsifying basis and TwIST reconstruction algorithm to be best.

Under optimized conditions, the CSSPIS approach can be significantly faster (orders of magnitude in detector noise limited cases) than the traditional pixel-by-pixel scanning counterpart because of the compression and multiplexing properties. Furthermore, while the measurements here were performed under non-gated continuous detection, DMDs have the potential to allow synchronized gated detection of pulsed plasmas with high temporal resolution, as demonstrated for LIBS,[40] which would lead to improved SBR and lateral resolution in GDOES EM.[9] Ultimately, the CSSPIS strategy is also amenable for being adapted to a potential implementation on

 This journal is © The Royal Society of Chemistry 2022

Published on 18 February 2022. Downloaded by Texas Tech University on 3/16/2022 9:08:21 PM.

readily available commercial GDOES instruments to allow multi-EM capabilities.

It is worth noting that array detectors can make CS spectral imaging approaches much more powerful by allowing many combinations to be measured at the same time and having simultaneous access to the wavelength dimension, which results in much faster imaging with multi-elemental capabilities. Thus, current work in the PI lab is already underway to incorporate an array detector and enable coded aperture snapshot spectral imaging (CASSI)[19,41] with the ultimate capability of capturing a full hyperspectral data cube in a single snapshot.

Conflicts of interest

There are no conflicts of interest to declare.

Acknowledgements

The authors would like to acknowledge support by the National Science Foundation under CHE-1610849 and CHE-2108359. In addition, the authors would like to thank S. Hiemstra and C. Pfeiffer at the TTU Dept. of Chemistry and Biochemistry Machine Shop for technical support. K. F. would like to acknowledge the ACS Division of Analytical Chemistry for its graduate fellowship support sponsored by the SACP.

References

1 M. Cruz-Alonso, A. Lores-Padín, E. Valencia, H. González-Iglesias, B. Fernández and R. Pereiro, *Anal. Bioanal. Chem.*, 2019, **411**, 549–558.
2 G. Gamez and K. Finch, *Spectrochim. Acta, Part B*, 2018, **148**, 129–136.
3 D. Hartnell, W. Andrews, N. Smith, H. Jiang, E. McAllum, R. Rajan, F. Colbourne, M. Fitzgerald, V. Lam, R. Takechi, M. J. Pushie, M. E. Kelly and M. J. Hackett, *Front. Neurosci.*, 2020, **13**, 1415.
4 A. Limbeck, L. Brunnbauer, H. Lohninger, P. Pořízka, P. Modlitbová, J. Kaiser, P. Janovszky, A. Kéri and G. Galbács, *Anal. Chim. Acta*, 2021, **1147**, 72–98.
5 E. J. McAllum and D. J. Hare, *Spectrochim. Acta, Part B*, 2019, **156**, 20–32.
6 G. Qian, Y. Li and A. R. Gerson, *Surf. Sci. Rep.*, 2015, **70**, 86–133.
7 A. van der Ent, W. J. Przybyłowicz, M. D. de Jonge, H. H. Harris, C. G. Ryan, G. Tylko, D. J. Paterson, A. D. Barnabas, P. M. Kopittke and J. Mesjasz-Przybyłowicz, *New Phytol.*, 2018, **218**, 432–452.
8 M. R. Webb, V. Hoffmann and G. M. Hieftje, *Spectrochim. Acta, Part B*, 2006, **61**, 1279–1284.
9 G. Gamez, S. Ray, F. Andrade, M. Webb and G. Hieftje, *Anal. Chem.*, 2007, **79**, 1317–1326.
10 G. Gamez, D. Frey and J. Michler, *J. Anal. At. Spectrom.*, 2012, **27**, 50–55.
11 G. Gamez, G. Mohanty and J. Michler, *J. Anal. At. Spectrom.*, 2013, **28**, 1016–1023.
12 G. Gamez, G. Mohanty and J. Michler, *J. Anal. At. Spectrom.*, 2014, **29**, 315–323.
13 M. Kroschk, J. Usala, T. Addesso and G. Gamez, *J. Anal. At. Spectrom.*, 2016, **31**, 163–170.
14 A. P. Storey, S. J. Ray, V. Hoffmann, M. Voronov, C. Engelhard, W. Buscher and G. M. Hieftje, *Appl. Spectrosc.*, 2017, **71**, 1280–1288.
15 M. Voronov, V. Hoffmann, T. Wallendorf, S. Marke, J. Mönch, C. Engelhard, W. Buscher, S. J. Ray and G. M. Hieftje, *J. Anal. At. Spectrom.*, 2012, **27**, 419–425.
16 G. Gamez, M. Voronov, S. Ray, V. Hoffmann, G. Hieftje and J. Michler, *Spectrochim. Acta, Part B*, 2012, **70**, 1–9.
17 G. Gamez, *J. Anal. At. Spectrom.*, 2016, **31**, 2165–2174.
18 M. Rani, S. B. Dhok and R. B. Deshmukh, *IEEE Access.*, 2018, **6**, 4875–4894.
19 G. R. Arce, D. J. Brady, L. Carin, H. Arguello and D. S. Kittle, *IEEE Signal Process. Mag.*, 2014, **31**, 105–115.
20 R. G. Baraniuk, *IEEE Signal Process. Mag.*, 2007, **24**, 118–120.
21 K. Bryan and T. Leise, *SIAM Rev.*, 2013, **55**, 547–566.
22 E. J. Candès, J. Romberg and T. Tao, *IEEE Trans. Inf. Theory*, 2006, **52**, 489–509.
23 E. J. Candès, J. K. Romberg and T. Tao, *Commun. Pure Appl. Math.*, 2006, **59**, 1207–1223.
24 D. L. Donoho, *IEEE Trans. Inf. Theory*, 2006, **52**, 1289–1306.
25 B. Hayes, *Am. Sci.*, 2009, **97**, 276–280.
26 D. J. Holland and L. F. Gladden, *Angew. Chem., Int. Ed.*, 2014, **53**, 13330–13340.
27 R. M. Willet, R. F. Mareia and J. M. Nichols, *Opt. Eng.*, 2011, 50.
28 J. D. Usala, A. Maag, T. Nelis and G. Gamez, *J. Anal. At. Spectrom.*, 2016, **31**, 2198–2206.
29 X. Cai, B. Hu, T. Sun, K. F. Kelly and S. Baldelli, *J. Chem. Phys.*, 2011, 135.
30 P. Duan, Y. Wang, D. Xu, C. Yan, Z. Yang, W. Xu, W. Shi and J. Yao, *Appl. Opt.*, 2016, **55**, 3670–3675.
31 M. F. Duarte, M. A. Davenport, D. Takbar, J. N. Laska, T. Sun, K. F. Kelly and R. G. Baraniuk, *IEEE Signal Process. Mag.*, 2008, **25**, 83–91.
32 J. Greenberg, K. Krishnamurthy and D. Brady, *Opt. Lett.*, 2014, **39**, 111–114.
33 V. Studera, J. Bobin, M. Chahida, H. S. Mousavia, E. Candes and M. Dahane, *Proc. Natl. Acad. Sci. U. S. A.*, 2012, **109**, E1679–E1687.
34 D. Takhar, J. N. Laska, M. B. Wakin, M. F. Duarte, D. Baron, S. Sarvotham, K. F. Kelly and R. G. Baraniuk, *Proc. SPIE-Int. Soc. Opt. Eng.*, 2006, 6065.
35 J. A. Tropp and S. J. Wright, *Proc.–IEEE*, 2010, **98**, 948–958.
36 J. M. Bioucas-Dias and M. A. T. Figueiredo, *IEEE Transactions on Image Pro.*, 2007, **16**, 2992–3004.
37 M. A. T. Figueiredo, R. D. Nowak and S. J. Wright, *IEEE J. Sel. Top. Signal Process.*, 2007, **1**, 586–597.
38 Z. Wang and A. C. Bovik, *IEEE Signal Process. Mag.*, 2009, **26**, 98–117.
39 A. K. Venkataramanan, C. Wu, A. C. Bovik, I. Katsavounidis and Z. Shahid, *IEEE Access.*, 2021, **9**, 28872–28896.
40 K. L. Williams, G. C. Y. Chan and S. J. Ray, *Spectrochim. Acta, Part B*, 2021, 179.
41 A. Wagadarikar, R. John, R. Willett and D. Brady, *Appl. Opt.*, 2008, **47**, B44–B51.